THE JOURNAL OF PHYSICAL CHEMISTRY C

Article

Cite This: J. Phys. Chem. C 2019, 123, 24818−24825

pubs.acs.org/JPCC

Dynamics of Defects in van der Waals Epitaxy of Bismuth Telluride Topological Insulators

Sérgio L. Morelhão,*[†,‡] Stefan W. Kycia,*[†] Samuel Netzke,[†] Celso I. Fornari,[§] Paulo H. O. Rappl,[§] and Eduardo Abramof[§]

[†]Department of Physics, University of Guelph, Guelph, Ontario N1G 1W2, Canada

[‡]Institute of Physics, University of São Paulo, São Paulo 05508-090, Brazil

[§]National Institute for Space Research, São José dos Campos, São Paulo 12227-010, Brazil

Supporting Information

ABSTRACT: Potential applications in spintronics and quantum information processing have motivated much recent research in epitaxial films of bismuth telluride. This system is also an example of van der Waals (vdW) epitaxy, where the interface coherence between the film and substrate is based on vdW bonds instead of strong ionic or covalent bonds. Because of the weakness of the vdW bonds, the overall quality of the epitaxial films is difficult to control and structural defects are easily introduced with a significant impact on the electronic phase diagram of the epitaxial films. To elucidate the evolution of defects as a function of the growth parameters, we combine nondestructive methods for electrical and structural analysis, as well as to establish intercorrelations between structural features and density of free charge carriers. It clearly shows that point defects and twinned domains favor p-type of charge carriers. Passivation of points defects by formation of metallic bismuth bilayers (BLs) drastically changes the whole film properties. By replacing vdW bonds with weak covalent bonds, the presence of BLs increases the film stiffness, leading to a smaller lattice misfit and a larger lateral lattice coherence length. Charge carriers are flipped to n-type. A few percent of BLs can be a strategy to achieve films with enhanced performance for device applications.

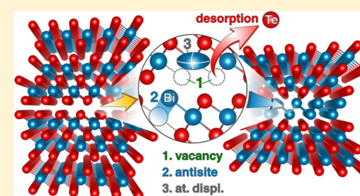

Downloaded via UNIV OF SAO PAULO on November 18, 2020 at 15:06:01 (UTC).
See https://pubs.acs.org/sharingguidelines for options on how to legitimately share published articles.

INTRODUCTION

van der Waals (vdW) epitaxy of bismuth chalcogenides has recently regained significant interest because of the possibility of suppressing bulk conduction in archetypes of 3D topological insulators.[1,2] Spin-polarized currents flowing exclusively through surface states in high-quality thin films can provide a basic platform for novel physics and devices.[3−10] Although weak vdW interactions play a fundamental role in emerging fields of 2D materials and materials-by-design,[11−13] the combination of atomic layers of distinct materials without lattice matching suffers from the absence of strong interlayer forces to dictate lateral order in the heterostructures. As a consequence, the overall quality of the epitaxial films are difficult to control.[14−16] Even in the case of systems with excellent lattice matching, such as bismuth telluride on BaF_2 substrate, structural defects are easily introduced with significant impact on the electronic phase diagram of the epitaxial films.[17] Systematic investigation on film characteristic versus growth parameters can provide a general road map for obtaining films with the desired bulk insulating behaviour.[4,18,19] However, it is extremely important to understand the key features behind such subtle sources of structural defects. Distinguishing features related to the weakness of vdW forces, and hence relevant to most systems based on vdW epitaxy, from features specifically related to other particularities of this system.

In this work, several X-ray diffraction tools are combined to investigate defects in bismuth telluride films grown by molecular beam epitaxy (MBE).[20,21] Intrinsic topological surface states have already been observed in such films,[22] making them good candidates for applications in spintronics or quantum computing.[23−28] The Bi_2Te_3 phase is formed by stacks of quintuple layers (QLs) coupled to each other along the growth direction by weak vdW interactions, Figure 1a. Compositional fluctuation, twinned domains, and bulk free carriers are among the main problems reported in these films.[16,17,20−22,29] Desorption of tellurium is the root of compositional fluctuation. However, from tellurium vacancies to bismuth-rich phases, there is a whole gamut of possible processes involved.[30] Antisite occupation can follow the introduction of vacancies in the vdW gaps, Figure 1b, promoting films full of point defects detrimental to lattice perfection. At some instant, lattice energy is minimized by turning point defects into bismuth bilayers (BLs),[20,21] Figure 1c. This is a critical instant in terms of free carriers as films with only point defects, only BLs, or coexisting point defects and BLs may have completely different behaviors. Twinned domains can be a simple consequence of low degree of lateral ordering in vdW epitaxy, or of any other source of lateral

Received: June 5, 2019
Revised: September 17, 2019
Published: September 19, 2019

ACS Publications © 2019 American Chemical Society

DOI: 10.1021/acs.jpcc.9b05377
J. Phys. Chem. C 2019, 123, 24818−24825

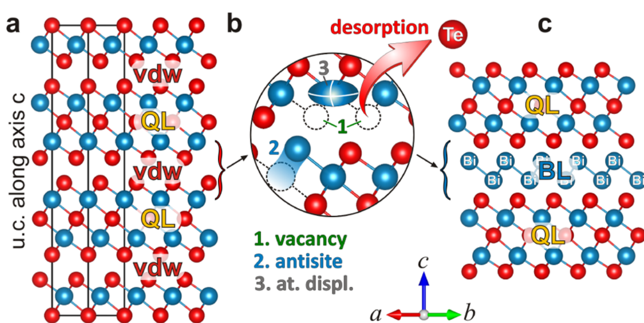

Figure 1. (a) Hexagonal unit cell (u.c.) of Bi_2Te_3 formed by stacking of three QLs coupled by weak vdW forces along the *c*-axis; viewing from the [110] direction (arrows along the basis vectors ***a***, ***b***, and ***c*** of the unit cell). (b) Desorption of Te during epitaxial growth introduces vacancies in the film structure, increasing antisite occupation and atomic displacements (at. displ.). (c) High atomic mobility allowing passivation of vacancies and antisites by formation of bismuth BLs in the vdW gaps.

inhomogeneities still to be identified. Moreover, lattice misfit can be slightly different in bismuth-rich films,[20,31] giving the opportunity to study the actual impact of lattice misfit in vdW epitaxy.

There is only one analytical tool capable of detecting the very small lattice misfit typical of this particular system, which is X-ray diffraction of hybrid reflections.[31−39] By using nondestructive analytical tools, the astonishing 0.002% accuracy of hybrid reflections can be combined with the ability of asymmetric reflections in grazing incidence geometry to access lattice coherence lengths and atomic displacement parameters regarding film lateral directions. Film composition, also from X-ray diffraction, and density of charge carriers from Hall effect complete the data set necessary to elucidate the intercorrelations between structural defects, mechanical and electrical properties of the films, allowing a deeper understanding on the role of bismuth BLs in such properties and of the lateral order in vdW epitaxy.

■ METHODS

Material Synthesis. Bismuth telluride films have been grown on BaF_2 (111) substrates using a Riber 32P MBE system.[21,22] Besides a nominal Bi_2Te_3 effusion cell, there are two additional sources of Te. The ratio Φ between beam equivalent pressures of Te and Bi_2Te_3 sources can be adjusted to compensate for the loss of tellurium during growth. Initially, a batch of samples with films grown at different substrate temperatures T_{sub} was prepared, but only samples with films presenting a single phase (Figure 2) were further analyzed. The main samples analyzed here are described in Table 1 with respect to growth parameters and measured film properties. All films were grown for 2 h at a constant rate of 0.22 Å/s, resulting in thicknesses of around 160 nm, as verified either by X-ray reflectometry[22,40] or cross-sectional scanning electron microscopy. Density and type of free charge carriers were obtained by the Hall effect.[17] The films grow in the trigonal crystal system, space group $R\bar{3}m$, with the (001) planes stacked along the growth direction.[41−45] The in-plane orientation of the films are such that the $\bar{1}0.20$ film reflection falls close to the 331 substrate reflection in reciprocal space,[22] or in terms of real space in-plane directions, $[110]Bi_2Te_3(001)\|[0\bar{1}1]$-$BiF_2(111)$,[31] see also Supporting Information S1.

X-ray Diffraction. X-ray data acquisition was carried out by a Huber four-circle diffractometer sourced by a fine focus copper rotating anode configured with a double collimating multilayer optic followed by a double bounce Ge 220 channel cut monochromator. The bandwidth is 1.2 eV for Cu Kα_1 (λ = 1.540562 Å). The dead time of the sodium-iodide scintillation detector is τ = 2.10 μs; photon counting rates are then given by $I = I' \exp(\tau I')$ for the detector readout values I'. Polarization factor[46,47] for this particular setup is described in Supporting Information S3. Adjustment arcs in the goniometric head were used to orient the diffraction vector of the 222 BaF_2 reflection with the ϕ rotation axis of the diffractometer within an accuracy better than 0.01°. Axial (vertical) divergence is about three times the divergence of 0.005° in the horizontal diffraction plane. Beam cross section was trimmed down to 0.4 × 0.4 mm^2 and the detector slits were open wide to accept diffracted X-rays from the full size of the beam footprint at the sample surface. All samples have surface areas larger than 10 × 10 mm^2.

■ RESULTS AND DISCUSSION

We begin by screening the batch of samples (section Material Synthesis) for films with single phases. In previous studies,[17,21] film growth at substrate temperatures T_{sub} < 220 °C were compromised by the high surface sticking coefficient of Te. Occurrence of Te-rich phases at and above this temperature was unknown. By probing the 02 10 asymmetric reflection of

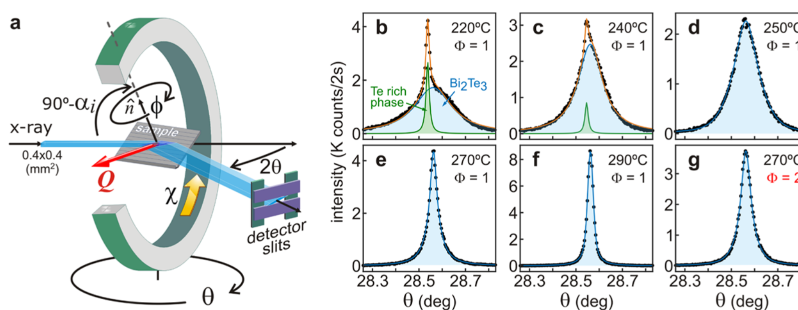

Figure 2. (a) X-ray footprint at the sample surface varying with θ and χ goniometer angles, $\alpha_i = \arcsin[\sin(\theta)\sin(\chi)]$ is the incidence angle. Normal direction $\hat{n}$ to both substrate (111) and film (001) planes is collinear with the rotation axis ϕ. Diffraction vector **Q** and the scattering angle 2θ are in the horizontal incidence plane. The incident beam cross section of 0.4 × 0.4 mm^2 providing diffracted beam with a few millimeter-stretched cross section in the incidence plane. (b−g) Rocking curves (θ-scans) of asymmetric 02 10 Bi_2Te_3 reflection in a series of films grown at different substrate temperatures and ratio Φ between beam equivalent pressures of Te and Bi_2Te_3 sources, as indicated beside each curve. Diffraction peak from reflection 02 2 of the Te hexagonal phase is still present for growth temperatures below 250 °C.

DOI: 10.1021/acs.jpcc.9b05377
J. Phys. Chem. C 2019, 123, 24818−24825

Table 1. Sample Labels, Ratio Φ of Beam Equivalent Pressure between Te and Bi_2Te_3 Sources, Substrate Temperature (T_{sub}), Film Thickness (t_f), In-Plane rms Atomic Displacement ($U_y^{1/2}$), Lattice Coherence Length (L_y), Lateral Lattice Mismatch ($\Delta a/a$), Allowed Elastic Strain (ε), Composition (Number of BLs per 100 QLs), Charge Carrier Density (c.d.), and Degree of Twinning $d_{tw} = P_{tw}/(P + P_{tw})$ (from Integrated Intensities in Figure 3a)

sample	Φ	T_{sub} (°C)	t_f (nm)	$U_y^{1/2}$ (pm)	L_y (nm)	$\Delta a/a$ (10^{-4})	ε (10^{-3})	BLs (%)	c.d. (10^{25}/m^3)	d_{tw} (%)
S15p	1	250	165 ± 2	14.80 ± 0.13	60 ± 6	−6.8 ± 1.0	6.6 ± 0.8		+9 ± 2	19.8 ± 0.3
S17n	1	270	154 ± 5	14.14 ± 0.39	158 ± 10	−1.1 ± 0.4	2.9 ± 0.2	9.4	−4 ± 1	35.5 ± 0.3
S19n	1	290	157 ± 10	13.87 ± 0.17	165 ± 14	+0.1 ± 0.3	2.6 ± 0.3	16.3	−40 ± 6	2.7 ± 0.1
S27p	2	270	160 ± 10	14.05 ± 0.31	81 ± 7	−5.6 ± 0.5	4.9 ± 0.5		+6 ± 1	44.3 ± 0.2

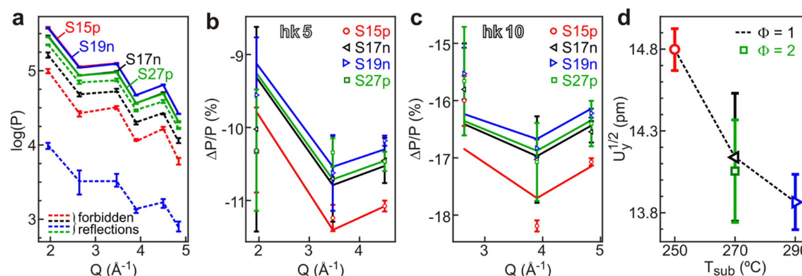

Figure 3. (a) Experimental (error bars) and best fitting (solid/dashed lines) values of integrated intensities P, peak areas in counts/s, of asymmetric $hk5$ and $hk10$ reflections in Bi_2Te_3 (001) films. Peak areas P_{tw} from forbidden reflections (dashed lines) owing to twinned domains are also shown. $Q = (4\pi/\lambda)\sin\theta_{hkl}$. (b,c) Relative variation of integrated intensities because of atomic displacement parameters, displayed separately in two graphs for the sake of clarity. $\Delta P/P = (P - P_0)/P_0$ where P stands either for experimental (symbols with error bars) or best fitting (solid lines) values. P_0 are the calculated values for null displacement parameters. (d) In-plane rms atomic displacement, $U_y^{1/2}$, from the data fitting shown as a function of substrate temperature T_{sub} during film growth and ratio Φ between beam equivalent pressures of Te and Bi_2Te_3 sources.

the Bi_2Te_3 film in non-coplanar diffraction geometry, Figure 2a, sharp peaks from reflection 02 2 of the hexagonal phase of Te are observed up to temperatures as high as 240 °C, Figure 2b,c, pushing up by about 20 °C the minimum T_{sub} for growing films free of Te-rich phases. The observed Te phase is epitaxial, has the same orientation of the Bi_2Te_3 lattice, and covers large areas of the samples as suggested by the sharpness of the peaks. The present study is focused on the single phase films, whose intensity curves $I(\theta)$ are shown in Figure 2d−g, corresponding to the samples labeled S15p, S17n, S19n, and S27p, respectively (Table 1).

Atomic Displacements. Changes in atomic displacement values as a function of the film growth parameters can be detected by measuring diffraction peak areas $P = \int I(\theta)d\theta$ of asymmetric reflections, such as those in Figure 2d−g. This procedure is suitable for thin films diffracting according to the kinematical theory of X-ray diffraction[48] as variation in peak widths (fwhm), as also seen in Figure 2d−g, can lead to correlated information on lattice coherence length along both lateral (in-plane) and longitudinal directions.

For this particular system, the choice of asymmetric reflections (Supporting Information S1) is based on diffraction vectors $\boldsymbol{Q}$ with large in-plane components, fixed angle of incidence α_i (Figure 2a), non-superposition with substrate reflections, and allowed/forbidden reflections obeying a threefold symmetry around the c-axis. Reflections with sixfold symmetry have mixed intensity contributions from both types of domains, normal and twinned,[21,22] avoiding quantitative analysis of twinned domains in the films. The integrated intensity data for all chosen reflections (allowed and forbidden) are shown in Figure 3a. Experimental values correspond to mean values from equivalent reflections that are set apart by 120° rotation in azimuth (ϕ axis), for example, reflections 20 10, $\bar{2}$2 10, and 0$\bar{2}$ 10 (or 20$\bar{2}$ 10, $\bar{2}$20 10, and 02$\bar{2}$ 10 in hexagonal four-index notation). Error bars are the standard errors of the mean values. Data fitting is obtained by adjusting effective values (same for all atoms) of lateral U_y, and longitudinal U_z, atomic displacements in the well-established integrated intensity expression of the kinematical theory (Supporting Information S2).

From the contributions of forbidden reflections in Figure 3a (dashed lines), we can see that all films have twinned domains. However, the film with the lowest amount of such domains, sample S19n, is also the one with the narrowest diffraction peaks, as in Figure 2f. Attempts to extract accurate values of atomic displacements were carried out by using the allowed reflections only. Goodness of fits are compared in Figure 3b,c, in terms of the relative variation $\Delta P/P = (P - P_0)/P_0$ of integrated intensities regarding calculated P_0 values with null atomic displacements (Supporting Information S2). Uncertainty in extracting atomic displacement values for each sample was estimated by repeating, several times, the data fitting with integrated intensity values randomly distributed within their error bars. This procedure reduced the uncertainty by a factor of 2 regarding simple error propagation for independent variables, that is, rms values of the relative errors. The obtained values of rms atomic displacements are comparable to the 16.4 (±0.6) pm ($U_{11} = U_{22} = 0.027 \pm 0.002$ Å^2) reported for the Te layers at the vdW gaps in bulk Bi_2Te_3 at 300 K,[49] confirming that the approach used here to calculate theoretical values is satisfactory at least to monitor relative variations from one sample to another. In films, the limited number of suitable reflections provide only an effective value for all atomic layers although, in the case of U_y, with enough accuracy to resolve a trend with the growth temperature, as can be seen in Figure 3d. On the other hand, longitudinal rms displacement $U_z^{1/2}$ = 14 (±2) pm in all films have poor accuracy because of the small variation of $Q_z = Q\cdot\hat{n}$ within the set of measured reflections, Q_z^2 = 1.06 Å^{-2} (l = 5) and 4.24 Å^{-2} (l = 10), hindering any observation of possible trends as a function of

DOI: 10.1021/acs.jpcc.9b05377
J. Phys. Chem. C 2019, 123, 24818−24825

the growth parameters. Determination of U_y with good reliability has been possible because of the choice of asymmetric reflections, covering diffraction vectors with very distinct in-plane components, Q_y^2 = 2.74, 11.0, and 19.2 Å^{-2}. In addition, each set of *hk*5 and *hk*10 reflections diffracts at a constant angle of incidence, α_i = 7.26° and 14.63°, respectively. It minimizes the susceptibility of the intensity data sets to the particular surface morphology of each film, as observed in a previous study.[50]

The simplest structure model of defects able to account for the observed increasing of atomic displacements at 250 °C is based on antisite occupation, as outlined in Figure 4 (inset).

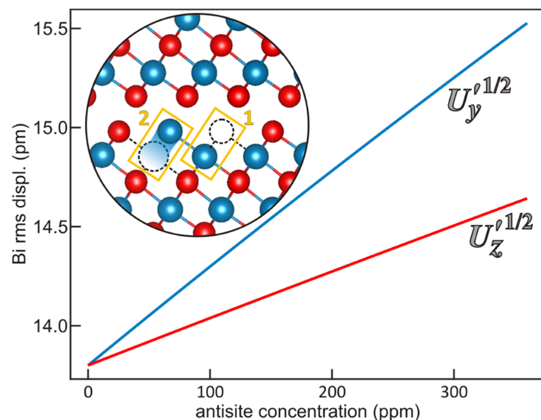

Figure 4. Lateral $U_y'^{1/2}$ and longitudinal $U_z'^{1/2}$ rms displacements of Bi ions because of antisite occupation of Te vacancies, as given by eq 1. Inset: Te vacancy (highlighted area 1) in the vdW gap and Bi ion (highlighted area 2) occupying a Te vacancy.

Te vacancies alone without causing significant displacement at neighboring sites are unable to increase the effective values of atomic displacements. A fraction ν of Bi ions moving to Te vacancies leads to $\langle \mathbf{r} \rangle = \nu \mathbf{r}_1 + (1 - \nu)\mathbf{r}_2$ as the mean atomic position of the Bi ions. $\mathbf{r}_1$ are vacancy positions at Te sites in the vdW gap, and $\mathbf{r}_2$ are adjacent positions of Bi sites such that $|\mathbf{r}_2 - \mathbf{r}_1|$ = 3.074 Å. The mean square displacements for Bi ions are then given by

$$U_k' = \nu |(\mathbf{r}_1 - \langle \mathbf{r} \rangle)\cdot\hat{\mathbf{k}}|^2 + (1 - \nu)|(\mathbf{r}_2 - \langle \mathbf{r} \rangle)\cdot\hat{\mathbf{k}}|^2 + U_{k,0} \quad (1)$$

either for $k = y$ or z. In-plane component of the diffraction vector $\mathbf{Q}$ is along direction $\hat{y}$, and $\hat{z}$ is parallel to the surface normal direction $\hat{n}$. By using $U_{y,0}^{1/2} = U_{z,0}^{1/2}$ = 13.8 pm from sample S19n as the minimum values due only to thermal vibration at room temperature, lateral and longitudinal rms displacements of Bi ions as a function of antisite concentration, $2\nu/5$, are shown in Figure 4. According to this model, the lateral displacement is much more susceptible to antisite occupation than the longitudinal one. The increase in $U_y^{1/2}$ from 13.8 pm (sample S19n) to 14.8 pm (sample S15p) in Figure 3d requires a minimum antisite concentration of 200 ppm as the experimental values are effective values for all atoms and not only for the Bi ions. In the Bi_2Te_3 structure, each element accounts for nearly 50% of the number of electrons, implying that the actual antisite occupation has to be at least twice this minimum value to produce an effective increase of $\Delta U_y^{1/2} \approx 1.0$ pm.

Lattice Coherence Lengths. In non-coplanar asymmetric diffraction geometry where the incidence plane is at an angle χ ≪ 90° from the film surface, rocking curve widths can also be correlated to the lateral lattice coherence length L_y, instead of only to the other coherence lengths, L_x and L_z, as schematized in Figure 5a. For the measured sets of *hk* 5 and *hk* 10

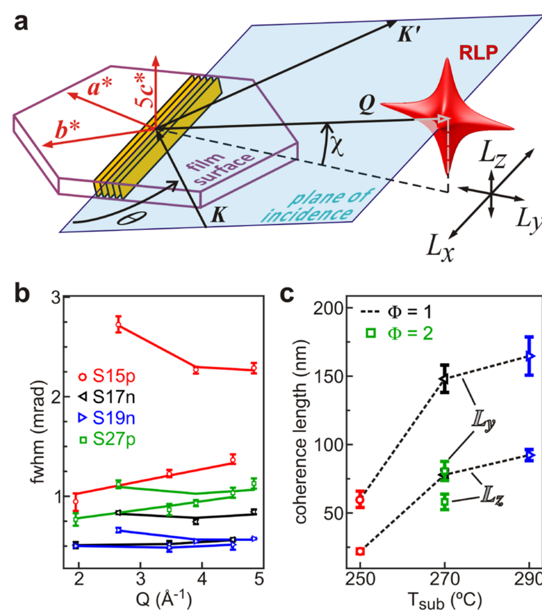

Figure 5. (a) Diffraction geometry of asymmetric reflection with diffraction vector $\mathbf{Q} = \mathbf{K}' - \mathbf{K}$ at an angle χ from the film surface, and extent of reciprocal lattice point because of finite lattice coherence lengths L_x and L_y (along film in-plane directions), and L_z (along the film growth direction) in the hexagonal film with reciprocal lattice of basis vectors $\mathbf{a}^*$, $\mathbf{b}^*$, and $\mathbf{c}^*$. $\mathbf{K}$ and $\mathbf{K}'$ stand for incident and diffracted X-ray wavevectors, respectively. (b) Experimental (symbols with error bars) and best fitting (solid lines) peak widths of *hk*5 and *hk*10 asymmetric reflections. (c) Lateral, L_y, and longitudinal, L_z, lattice coherence lengths extracted from the data fitting of peak widths as a function of the growth parameters T_{sub} and Φ.

asymmetric reflections, their observed peak widths are summarized in Figure 5b where experimental values correspond to mean values from equivalent reflections, error bars are the standard errors of the mean values, and best fitting data of peak widths were obtained by adjusting for each set of reflections the lattice coherence lengths in an easy-to-use peak width function given by

$$w_S = \frac{5.566}{Q}\sqrt{\frac{1}{L_x^2} + \tan^2\theta\left(\frac{\cos^2\chi}{L_y^2} + \frac{\sin^2\chi}{L_z^2}\right)} \quad (2)$$

as described in Supporting Information S4. Besides the overall dependence with the growth parameters, each set of reflections presents distinct behaviors as a function of Q. In agreement with eq 2, these distinct behaviors can be observed when the peak broadening because of coherence length L_x is negligible, that is $L_x \gg L_{y,z}$. In fact, data fitting shows no resolution to L_x, with values scattered over a wide range above a few microns. On the other hand, the values of L_y and L_z have clear trends with the growth parameters as shown in Figure 5c.

As the coherence length L_x stands for a direction perpendicular to the diffraction vector, all lattice imperfections present in the films have Burger vectors[51] either lying on the Bragg planes or along orthogonal directions to L_x. In other words, along the direction of L_x, the Bragg planes are

DOI: 10.1021/acs.jpcc.9b05377
J. Phys. Chem. C 2019, 123, 24818−24825

diffracting in a phase even across domain boundaries and twinned domains, showing no evidence of in-plane lattice misorientation of the main domains covering the films.

The longitudinal coherence length L_z can be related to the presence of stacking faults of QLs parallel to the film surface.[6] However, as both coherence length L_y and L_z present similar trends with the growth parameters in Figure 5c, stacking faults may be taking place on inclined planes and, in this case, their cause might be related to the film/substrate lattice misfit.

Lateral Lattice Mismatch. In conventional epitaxy where atomic layers are strongly bound to each other along the growth direction, as well as across the interface, the lateral lattice coherence length L_y is dictated by the mean separation distance of lattice imperfections,[52,53] such that

$$L_y \approx a_s/(\varepsilon + |\Delta a/a|) \quad (3)$$

where ε is the amount of lattice misfit that can be elastically accommodated, and $\Delta a/a = (a_f - a_s)/a_s$ is the actual lattice mismatch present in the sample with respect to the film and substrate lateral lattice parameters, a_f and a_s, respectively.

In this epitaxial system, besides the lateral lattice mismatch being very small, it is also known that $\Delta a/a \simeq +4 \times 10^{-4}$ regarding bulk values,[49] $\Delta a/a \lesssim -1 \times 10^{-4}$ in relaxed films,[20,31] and that $\Delta a/a$ varies with the presence of bismuth BLs (Figure 1c) in the films.[31] It implies that to resolve any possible trend with the growth parameters, a very accurate tool to measure $\Delta a/a$ is needed. Measuring hybrid reflection pairs is the proper method as its accuracy can be as good as 2×10^{-5} in this particular epitaxial system.[31] The reason for such extreme accuracy is summarized in Figure 6a,b. In a hybrid path of two consecutive reflections, one in the film ($\mathbf{Q}_f$) and the other in the substrate ($\mathbf{Q}_s$) lattice, the resulting diffraction vector $\mathbf{Q}^* = \mathbf{Q}_f + \mathbf{Q}_s$ is lined up with the surface normal direction, unless $\Delta a/a \neq 0$. For $\Delta a/a < 0$, $\mathbf{Q}^*$ shifts toward lower diffraction angles (Figure 6a), whereas for the opposite sequence of reflections, $\mathbf{Q}^* = \mathbf{Q}_s + \mathbf{Q}_f$, it shifts toward higher angles (Figure 6b). By measuring such a pair of hybrid reflections with opposite sequences, the split on their peak positions is directly related to $\Delta a/a$. For the pair we choose to measure in Figure 6c, this relationship is given by $\Delta\theta = \theta_{s/f} - \theta_{f/s} = -2.035\Delta a/a$ (Supporting Information S5). Figure 6d shows the measured lattice mismatches as a function of the growth parameters.

Final Results. There is an undeniable correlation in qualitative terms between the coherence lengths in Figure 5c and the lattice mismatch in Figure 6d. Observation of such correlation is a remarkable achievement. Two completely distinct methods were used to access these quantities; one method is based on analysis of peak widths in asymmetric diffraction geometry, whereas the other depends on peak splitting of hybrid reflections in symmetric diffraction geometry. Even so, these results agree, showing similar trends with the growth parameters in accordance with eq 3. From the quantitative point of view, to match both results, the elastic properties of the films have to be changing, as implied by the amount ε of elastic strain each film can handle. Figure 6d also shows the values of ε determined from L_y and $\Delta a/a$ through eq 3. Smaller the value of ε stiffer the film, resulting in smaller lattice mismatch and, consequently, larger lateral lattice coherence lengths. As all films have nearly the same thickness, changes in mechanical properties can be caused by formation of bismuth BLs in the vdW gaps of films with composition $(Bi_2)_M(Bi_2Te_3)_N$ where M is the number of BLs per number N

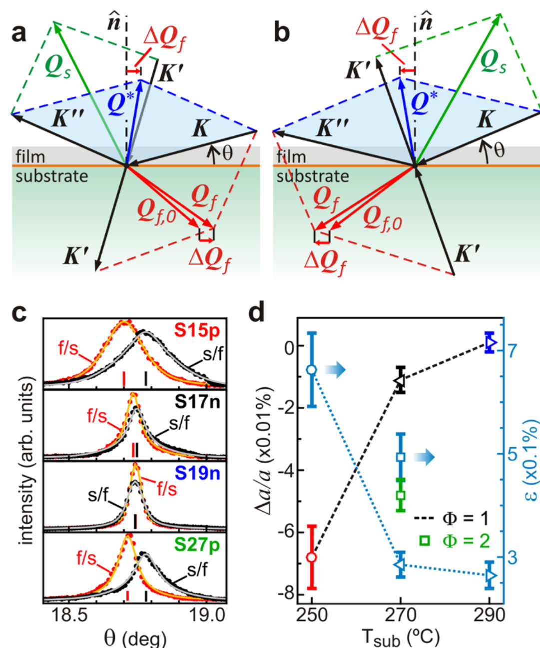

Figure 6. (a,b) Scheme of hybrid reflection pair used to access lateral lattice mismatch $\Delta a/a$ in Bi_2Te_3 films;[31] (a) $\mathbf{Q}^* = \mathbf{Q}_f + \mathbf{Q}_s$ and (b) $\mathbf{Q}^* = \mathbf{Q}_s + \mathbf{Q}_f$ where the order of sums indicates the sequence of consecutive reflections. Tilting of vectors $\mathbf{Q}^*$ occur when $\Delta a/a \neq 0$ as $\Delta\mathbf{Q}_f = \mathbf{Q}_f - \mathbf{Q}_{f,0} \propto \Delta a/a$. Wavevectors $\mathbf{K}$, $\mathbf{K}'$, and $\mathbf{K}''$ stand for incident beam, and 1st and 2nd diffracted beams, respectively. (c) Observed splitting of hybrid peaks in the samples (S15p, S17n, S19n, and S27p): $\bar{2}2\,\bar{1}0_f + 044_s$ (peak f/s) and $404_s + 0\bar{2}\,\bar{1}0_f$ (peak s/f).[31] (d) Lateral lattice mismatch determined from the observed splitting of hybrid peaks as a function of film growth parameters T_{sub} and Φ. Elastic strains, ε in eq 3, are indicated at the scale on the right.

of QLs. $Bi_2Te_{3-\delta}$ stands for the film composition in terms of Te deficit $\delta = 3M/(M + N)$. Concentration of BLs in the films were measured by comparing experimental and simulated X-ray diffraction data, as described in Supporting Information S6. The determined values of BL concentration are presented in Table 1 (column 9). On top of all this, there is still the fact that charge carrier type and density are changing in the films, as characterized elsewhere.[17] These last results together with all others are summarized in Table 1.

All results combined reveal the underlying dynamic of defects responsible for the strong correlation between film properties and growth parameters. Above the minimum temperature to avoid formation of Te-rich phases (~240 °C), desorption of Te starts to introduce vacancies in the growing film. At 250 °C, vacant Te sites have been occupied by Bi ions as suggested by the higher value (regarding the other films) of rms atomic displacement measured at room temperature. Antisite concentration is estimated to be around 400 ppm, and the relatively small lattice coherence length of 60 nm collaborates with the scenario of low atomic mobility where point defects (antisites) are trapped in the film structure. Lattice mismatch is close to values reported for relaxed $Bi_2Te_{3-\delta}$ films with no significant deficit of Te ($\delta < 0.001$).[20,31] During growth at 270 and 290 °C, production of vacancies leads to huge deficits of Te ($\delta \approx 0.26$ and 0.42, corresponding to 9.4 and 16.3 BLs in 100 QLs, respectively). However, a much higher concentration of antisites plus a rise in thermal energy favor formation of BLs, which seems to minimize lattice disorder as there are perceptible reductions of

DOI: 10.1021/acs.jpcc.9b05377
J. Phys. Chem. C 2019, 123, 24818−24825

about 0.8 ± 0.3 pm in the rms values of atomic displacement. Well-resolved changes in film stiffness points toward strengthening of interlayer forces when weak QL::QL vdW bonds are replaced by stronger bonds between the BLs and the nearest Te atoms in adjacent QLs, QL:BL:QL.

In the homologous series of bulk Bi_mTe_n phases, the lattice parameter *a* (lateral in the films) increases with the BL content.[10,20] In the films, the slightly larger in-plane atomic distances in the BLs promote an increase in the lateral lattice parameter, which is detected here as a reduction of lattice mismatch. Both effects of strengthening interlayer forces and reducing lattice mismatch seem to be key features to improve by a factor of 2 or 3 the film lateral order, that is the lateral lattice coherent lengths. A drastic reduction in the degree of twinning (Table 1, column 11) is observed for the film presenting practically null lattice mismatch. By doubling the Te offer during growth at 270 °C, desorption is suppressed, no increase of rms displacement is noticed, and the Bi_2Te_3 phase with no deficit of tellurium is obtained. However, without BLs lattice mismatch increases in amplitude and the film lateral order recedes. Although the temperature of growth can affect the degree of twinning, comparison of the amount of twinning in both films grown under the same temperature suggests that interlayer forces and lattice mismatch are in fact playing a role in minimizing the formation of twinned domains. It is well known that formation of defects are difficult to be suppressed in incommensurate epitaxy on substrates other than BaF_2(111).[43] However, to fully understand the role of very small lattice mismatches in the degree of twinning, further investigation would be necessary. It may include variation of other growth parameters, such as the growth rate that was kept constant in the set of samples investigated here.

■ CONCLUSIONS

Structural, mechanical, and electrical properties of bismuth telluride epitaxial films are ruled by the competition between desorption of tellurium and interlayer atomic mobility during growth. Desorption without enough mobility leads to point defects such as Te vacancies and antisites with Bi ions occupying Te sites. Concentration of antisites to levels of a few hundreds ppm can produce a slight but detectable increase of rms atomic displacements. With enough atomic mobility, point defects are passivated by the formation of bismuth BLs, which turns to trigger major changes in the film properties. Films become stiffer and with smaller lattice mismatch, resulting in improvement of the lateral order (lateral lattice coherence length). Except for the film growing under slow mobility conditions, higher the lateral order smaller the amount of twinned domains. Point defects seem to favor p-type of charger carriers, which quickly change to n-type when the point defects turn into bismuth BLs. It suggests that in the electronic phase diagram,[17] the flip between p- and n-types of charge carries is driven by the presence of metallic bismuth BLs. Total suppression of BLs is possible by using additional sources of tellurium to prevent desorption. However, in the absence of BLs film stiffness recedes, resulting in larger lattice mismatch and reduction of lateral order that favors twinned domains and p-type of charge carrier. Allowing a low percentage of bismuth BLs in the structure can be a good strategy to obtain films with bulk insulating behavior and enhanced surface spin polarized currents for application in spintronic devices.

The role of lattice misfit in vdW epitaxy has been better understood with the help of an important X-ray tool introduced here. Combined with other tools previously used,[31,50] access to lattice coherence lengths by measuring asymmetric reflections revealed that lattice mismatch leads to film imperfection such as stacking faults and twinned domains. Also, it provides information on mechanical properties in terms of the amount of strain that can be elastically accommodated by films of slightly different compositions.

■ ASSOCIATED CONTENT

Supporting Information

The Supporting Information is available free of charge on the ACS Publications website at DOI: 10.1021/acs.jpcc.9b05377.

Choice of asymmetric reflections, integrated intensity expression and atomic displacement parameters, polarization factor for the used X-ray diffractometer, lateral lattice coherence length in thin films, hybrid reflections, and film composition from X-ray diffraction in specular reflection geometry (PDF)

■ AUTHOR INFORMATION

Corresponding Authors

*E-mail: morelhao@if.usp.br (S.L.M.).
*E-mail: skycia@uoguelph.ca (S.K.).

ORCID

Sérgio L. Morelhão: 0000-0003-1643-0948

Author Contributions

C.I.F., P.H.O.R., and E.A. grew the epitaxial films, carried out charge carrier (Hall effect) and film thickness measurements. S.K. and S.L.M. developed the X-ray methods, data collection, and analysis procedures. S.N. contributed to X-ray measurements. The paper was written through contributions of all the authors.

Notes

The authors declare no competing financial interest.
Defects in vdW epitaxy of Bi_2Te_3.

■ ACKNOWLEDGMENTS

The authors acknowledge the financial support from Brazilian agencies CAPES (grant no. 88881.119076/2016-01), FAPESP (grant nos. 2016/22366-5 and 2018/00303-7), and CNPq (grant nos. 302134/2014-0, 309867/2017-7, and 305764/2018-7), as well as from the NSERC of Canada.

■ REFERENCES

(1) Hoefer, K.; Becker, C.; Rata, D.; Swanson, J.; Thalmeier, P.; Tjeng, L. H. Intrinsic conduction through topological surface states of insulating Bi2Te3epitaxial thin films. *Proc. Natl. Acad. Sci. U.S.A.* **2014**, *111*, 14979−14984.

(2) Guo, Y.; Liu, Z.; Peng, H. A Roadmap for Controlled Production of Topological Insulator Nanostructures and Thin Films. *Small* **2015**, *11*, 3290−3305.

(3) Hsieh, D.; Xia, Y.; Qian, D.; Wray, L.; Dil, J. H.; Meier, F.; Osterwalder, J.; Patthey, L.; Checkelsky, J. G.; Ong, N. P.; et al. A Tunable Topological Insulator in the Spin Helical Dirac Transport Regime. *Nature* **2009**, *460*, 1101−1105.

(4) Zhang, Y.; He, K.; Chang, C.-Z.; Song, C.-L.; Wang, L.-L.; Chen, X.; Jia, J.-F.; Fang, Z.; Dai, X.; Shan, W.-Y.; et al. Crossover of the Three-Dimensional Topological Insulator Bi2Se3 to the Two-Dimensional Limit. *Nat. Phys.* **2010**, *6*, 584−588.

(5) Wang, G.; Zhu, X.-G.; Sun, Y.-Y.; Li, Y.-Y.; Zhang, T.; Wen, J.; Chen, X.; He, K.; Wang, L.-L.; Ma, X.-C.; et al. Topological Insulator Thin Films of Bi2Te3 with Controlled Electronic Structure. *Adv. Mater.* **2011**, *23*, 2929−2932.

(6) Seixas, L.; Abdalla, L. B.; Schmidt, T. M.; Fazzio, A.; Miwa, R. H. Topological States Ruled by Stacking Faults in Bi2Se3 and Bi2Te3. *J. Appl. Phys.* **2013**, *113*, 023705.
(7) Ni, Y.; Zhang, Z.; Nlebedim, C. I.; Jiles, D. C. Magnetotransport study of (Sb1−xBix)2Te3 thin films on mica substrate for ideal topological insulator. *AIP Adv.* **2016**, *6*, 055812.
(8) Eschbach, M.; Lanius, M.; Niu, C.; Młyńczak, E.; Gospodarič, P.; Kellner, J.; Schüffelgen, P.; Gehlmann, M.; Döring, S.; Neumann, E.; et al. Bi1Te1 is a Dual Topological Insulator. *Nat. Commun.* **2017**, *8*, 14976.
(9) Kou, L.; Niu, C.; Fu, H.; Ma, Y.; Yan, B.; Chen, C. Tunable Quantum Order in Bilayer Bi2Te3: Stacking Dependent Quantum Spin Hall States. *Appl. Phys. Lett.* **2018**, *112*, 243103.
(10) Springholz, G.; Wimmer, S.; Groiss, H.; Albu, M.; Hofer, F.; Caha, O.; Kriegner, D.; Stangl, J.; Bauer, G.; Holý, V. Structural Disorder of Natural BimSenSuperlattices Grown by Molecular Beam Epitaxy. *Phys. Rev. Mater.* **2018**, *2*, 054202.
(11) Fiori, G.; Bonaccorso, F.; Iannaccone, G.; Palacios, T.; Neumaier, D.; Seabaugh, A.; Banerjee, S. K.; Colombo, L. Electronics Based on Two-Dimensional Materials. *Nat. Nanotechnol.* **2014**, *9*, 768−779.
(12) Bhimanapati, G. R.; Lin, Z.; Meunier, V.; Jung, Y.; Cha, J.; Das, S.; Xiao, D.; Son, Y.; Strano, M. S.; Cooper, V. R.; et al. Recent Advances in Two-Dimensional Materials beyond Graphene. *ACS Nano* **2015**, *9*, 11509−11539.
(13) Novoselov, K. S.; Mishchenko, A.; Carvalho, A.; Castro Neto, A. H. 2D Materials and van der Waals Heterostructures. *Science* **2016**, *353*, aac9439.
(14) He, L.; Kou, X.; Wang, K. L. Review of 3D Topological Insulator Thin-Film Growth by Molecular Beam Epitaxy and Potential Applications. *Phys. Status Solidi RRL* **2013**, *7*, 50−63.
(15) Schreyeck, S.; Tarakina, N. V.; Karczewski, G.; Schumacher, C.; Borzenko, T.; Brüne, C.; Buhmann, H.; Gould, C.; Brunner, K.; Molenkamp, L. W. Molecular Beam Epitaxy of High Structural Quality Bi2Se3 on Lattice Matched InP(111) Substrates. *Appl. Phys. Lett.* **2013**, *102*, 041914.
(16) Kampmeier, J.; Borisova, S.; Plucinski, L.; Luysberg, M.; Mussler, G.; Grützmacher, D. Suppressing Twin Domains in Molecular Beam Epitaxy Grown Bi2Te3 Topological Insulator Thin Films. *Cryst. Growth Des.* **2015**, *15*, 390−394.
(17) Fornari, C. I.; Rappl, P. H. O.; Morelhão, S. L.; Fornari, G.; Travelho, J. S.; de Castro, S.; Pirralho, M. J. P.; Pena, F. S.; Peres, M. L.; Abramof, E. Structural defects and electronic phase diagram of topological insulator bismuth telluride epitaxial films. *Mater. Res. Express* **2018**, *5*, 116410.
(18) Qi, X.-L.; Zhang, S.-C. Topological Insulators and Superconductors. *Rev. Mod. Phys.* **2011**, *83*, 1057−1110.
(19) Ando, Y. Topological Insulator Materials. *J. Phys. Soc. Jpn.* **2013**, *82*, 102001.
(20) Steiner, H.; Volobuev, V.; Caha, O.; Bauer, G.; Springholz, G.; Holý, V. Structure and Composition of Bismuth Telluride Topological Insulators Grown by Molecular Beam Epitaxy. *J. Appl. Crystallogr.* **2014**, *47*, 1889−1900.
(21) Fornari, C. I.; Rappl, P. H. O.; Morelhão, S. L.; Abramof, E. Structural Properties of Bi2Te3 Topological Insulator Thin Films Grown by Molecular Beam Epitaxy on (111) BaF2 Substrates. *J. Appl. Phys.* **2016**, *119*, 165303.
(22) Fornari, C. I.; Rappl, P. H. O.; Morelhão, S. L.; Peixoto, T. R. F.; Bentmann, H.; Reinert, F.; Abramof, E. Preservation of Pristine Bi2Te3 Thin Film Topological Insulator Surface After ex Situ Mechanical Removal of Te Capping Layer. *APL Mater.* **2016**, *4*, 106107.
(23) Moore, J. E. The Birth of Topological Insulators. *Nature* **2010**, *464*, 194−198.
(24) Konig, M.; Wiedmann, S.; Brune, C.; Roth, A.; Buhmann, H.; Molenkamp, L. W.; Qi, X.-L.; Zhang, S.-C. Quantum Spin Hall Insulator State in HgTe Quantum Wells. *Science* **2007**, *318*, 766−770.
(25) Pesin, D.; MacDonald, A. H. Spintronics and Pseudospintronics in Graphene and Topological Insulators. *Nat. Mater.* **2012**, *11*, 409−416.
(26) Akhmerov, A. R.; Nilsson, J.; Beenakker, C. W. J. Electrically Detected Interferometry of Majorana Fermions in a Topological Insulator. *Phys. Rev. Lett.* **2009**, *102*, 216404.
(27) Kong, D.; Randel, J. C.; Peng, H.; Cha, J. J.; Meister, S.; Lai, K.; Chen, Y.; Shen, Z.-X.; Manoharan, H. C.; Cui, Y. Topological Insulator Nanowires and Nanoribbons. *Nano Lett.* **2010**, *10*, 329−333.
(28) Peng, H.; Lai, K.; Kong, D.; Meister, S.; Chen, Y.; Qi, X.-L.; Zhang, S.-C.; Shen, Z.-X.; Cui, Y. Aharonov-Bohm Interference in Topological Insulator Nanoribbons. *Nat. Mater.* **2009**, *9*, 225−229.
(29) Hoefer, K.; Becker, C.; Wirth, S.; Hao Tjeng, L. Protective Capping of Topological Surface States of Intrinsically Insulating Bi2Te3. *AIP Adv.* **2015**, *5*, 097139.
(30) Hashibon, A.; Elsässer, C. First-Principles Density Functional Theory Study of Native Point Defects in Bi2Te3. *Phys. Rev. B: Condens. Matter Mater. Phys.* **2011**, *84*, 144117.
(31) Morelhão, S. L.; Kycia, S.; Netzke, S.; Fornari, C. I.; Rappl, P. H. O.; Abramof, E. Hybrid Reflections from Multiple X-ray Scattering in Epitaxial Bismuth Telluride Topological Insulator Films. *Appl. Phys. Lett.* **2018**, *112*, 101903.
(32) Morelhão, S. L.; Cardoso, L. P. Simulation of Hybrid Reflections in X-ray Multiple Diffraction Experiments. *J. Cryst. Growth* **1991**, *110*, 543−552.
(33) Morelhão, S. L.; Avanci, L. H.; Hayashi, M. A.; Cardoso, L. P.; Collins, S. P. Observation of Coherent Hybrid Reflection with Synchrotron Radiation. *Appl. Phys. Lett.* **1998**, *73*, 2194−2196.
(34) Hayashi, M. A.; Avanci, L. H.; Cardoso, L. P.; Bettini, J.; de Carvalho, M. M. G.; Morelhão, S. L.; Collins, S. P. High-Resolution Synchrotron Radiation Renninger Scan to Examine Hybrid Reflections in InGaP/GaAs(001). *J. Synchrotron Radiat.* **1999**, *6*, 29−33.
(35) Morelhão, S. L.; Domagala, J. Z. Hybrid Reciprocal Space for X-ray Diffraction in Epitaxic Layers. *J. Appl. Crystallogr.* **2007**, *40*, 546−551.
(36) Morelhão, S. L.; Quivy, A. A.; Härtwig, J. Hybrid and Effective Satellites for Studying Superlattices. *Microelectron. J.* **2003**, *34*, 695−699.
(37) de Prado, E.; Martínez-Tomás, M. C.; Deparis, C.; Muñoz-Sanjosé, V.; Zúñiga-Pérez, J. Hybrid multiple diffraction in semipolar wurtzite materials: (\bf 01\overline{1}2)-oriented ZnMgO/ZnO heterostructures as an illustration. *J. Appl. Crystallogr.* **2017**, *50*, 1165−1173.
(38) Smith, E. H.; King, P. D. C.; Soukiassian, A.; Ast, D. G.; Schlom, D. G. Hybrid Reflections from Multiple X-ray Scattering in Epitaxial Oxide Films. *Appl. Phys. Lett.* **2017**, *111*, 131903.
(39) Domagała, J. Z.; Morelhão, S. L.; Sarzyński, M.; Maździarz, M.; Dłużewski, P.; Leszczyński, M. Hybrid Reciprocal Lattice: Application to Layer Stress Determination in GaAlN/GaN(0001) Systems with Patterned Substrates. *J. Appl. Crystallogr.* **2016**, *49*, 798−805.
(40) Morelhão, S. L.; Brito, G. E. S.; Abramof, E. Nanostructure of sol-gel films by x-ray specular reflectivity. *Appl. Phys. Lett.* **2002**, *80*, 407−409.
(41) Lee, J. J.; Schmitt, F. T.; Moore, R. G.; Vishik, I. M.; Ma, Y.; Shen, Z. X. Intrinsic Ultrathin Topological Insulators Grown via Molecular Beam Epitaxy Characterized by *in-Situ* Angle Resolved Photoemission Spectroscopy. *Appl. Phys. Lett.* **2012**, *101*, 013118.
(42) Ginley, T.; Wang, Y.; Law, S. Topological Insulator Film Growth by Molecular Beam Epitaxy: A Review. *Crystals* **2016**, *6*, 154.
(43) Bonell, F.; Cuxart, M. G.; Song, K.; Robles, R.; Ordejón, P.; Roche, S.; Mugarza, A.; Valenzuela, S. O. Growth of Twin-Free and Low-Doped Topological Insulators on BaF2(111). *Cryst. Growth Des.* **2017**, *17*, 4655−4660.
(44) Kriegner, D.; Harcuba, P.; Veselý, J.; Lesnik, A.; Bauer, G.; Springholz, G.; Holý, V. Twin Domain Imaging in Topological Insulator Bi2Te3 and Bi2Se3 Epitaxial Thin Films by Scanning X-ray

DOI: 10.1021/acs.jpcc.9b05377
J. Phys. Chem. C 2019, 123, 24818−24825

Nanobeam Microscopy and Electron Backscatter Diffraction. *J. Appl. Crystallogr.* **2017**, *50*, 369−377.
(45) Wang, Y.; Ginley, T. P.; Law, S. Growth of high-quality Bi2Se3 topological insulators using (Bi1-xInx)2Se3 buffer layers. *J. Vac. Sci. Technol., B: Nanotechnol. Microelectron.: Mater., Process., Meas., Phenom.* **2018**, *36*, 02D101.
(46) Morelhão, S. L.; Avanci, L. H. Strength Tuning of Multiple Waves in Crystals. *Acta Crystallogr., Sect. A: Found. Crystallogr.* **2001**, *57*, 192−196.
(47) Morelhão, S. L.; Remédios, C. M. R.; Freitas, R. O.; dos Santos, A. O. X-ray Phase Measurements as a Probe of Small Structural Changes in Doped Nonlinear Optical Crystals. *J. Appl. Crystallogr.* **2011**, *44*, 93−101.
(48) Morelhão, S. L. *Computer Simulation Tools for X-ray Analysis; Graduate Texts in Physics*; Springer: Cham, 2016.
(49) Mansour, A. N.; Wong-Ng, W.; Huang, Q.; Tang, W.; Thompson, A.; Sharp, J. Structural characterization of Bi2Te3 and Sb2Te3 as a function of temperature using neutron powder diffraction and extended X-ray absorption fine structure techniques. *J. Appl. Phys.* **2014**, *116*, 083513.
(50) Morelhão, S. L.; Fornari, C. I.; Rappl, P. H. O.; Abramof, E. Nanoscale characterization of bismuth telluride epitaxial layers by advanced X-ray analysis. *J. Appl. Crystallogr.* **2017**, *50*, 399−410.
(51) Morelhão, S. L.; Härtwig, J.; Meier, D. L. Dislocations in Dendritic Web Silicon. *J. Cryst. Growth* **2000**, *213*, 288−298.
(52) van der Merwe, J. H. The Role of Lattice Misfit in Epitaxy. *Crit. Rev. Solid State Mater. Sci.* **1978**, *7*, 209−231.
(53) Herman, M. A.; Richter, W.; Sitter, H. *Epitaxy: Physical Principles and Technical Implementation*; Springer: Berlin, Heidelberg, 2004; pp 389−421.

DOI: 10.1021/acs.jpcc.9b05377
J. Phys. Chem. C 2019, 123, 24818−24825